2009

Non-Intrusive Temperature Measurements Using Microscale Visualization Techniques

Pramod Chamarthy

S V. Garimella
Purdue University, sureshg@purdue.edu

Chamarthy, Pramod and Garimella, S V., "Non-Intrusive Temperature Measurements Using Microscale Visualization Techniques" (2009). *CTRC Research Publications.* Paper 119.
http://dx.doi.org/10.1007/s00348-009-0646-1

Non-Intrusive Temperature Measurement Using Microscale Visualization Techniques

Pramod Chamarthy, Steven T. Wereley[¶] and Suresh V. Garimella
Cooling Technologies Research Center
School of Mechanical Engineering and Birck Nanotechnology Center
Purdue University, West Lafayette, Indiana 47907-2088 USA

ABSTRACT

μPIV is a widely accepted tool for making accurate measurements in microscale flows. The particles that are used to seed the flow, due to their small size, undergo Brownian motion which adds a random noise component to the measurements. Brownian motion introduces an undesirable error in the velocity measurements, but also contains valuable temperature information. A PIV algorithm which detects both the location and broadening of the correlation peak can measure velocity as well as temperature simultaneously using the same set of images. The approach presented in this work eliminates the use of the calibration constant used in the literature (Hohreiter et al. 2002) [1], making the method system-independent, and reducing the uncertainty involved in the technique. The temperature in a stationary fluid was experimentally measured using this technique and compared to that obtained using the particle tracking thermometry method (PTT) and a novel method, low image density PIV (LID-PIV). The method of cross-correlation PIV was modified to measure the temperature of a moving fluid. A standard epi-fluorescence μPIV system was used for all the measurements. The experiments were conducted using spherical fluorescent polystyrene-latex particles suspended in water. Temperatures ranging from 20ºC – 80ºC were measured. This method allows simultaneous non-intrusive temperature and velocity measurements in integrated cooling systems and lab-on-a-chip devices.

Keywords: μPIV, Brownian motion, non-intrusive temperature measurement

[¶] Author to whom correspondence should be addressed: 765-494-5624, wereley@purdue.edu

1. INTRODUCTION

The recent advances in MEMS and microfluidics have given rise to a growing interest in miniaturizing many chemical and biological processes. The use of microfluidic devices and sensors for these applications would reduce manufacturing and operation costs, and decrease reaction times and power requirements while utilizing smaller amounts of reagents. MEMS devices are currently being developed for a broad range of applications such as bio-chemical analysis [2] and diagnostics [3], production of organic compounds, combinatorial chemistry, multi-component analytical systems [4, 5], microreactors [6-9] and integrated chip cooling systems [10, 11], to name a few. As the number of potential applications has increased, it has become necessary to develop the tools and techniques required to properly characterize the components involved.

Several techniques have been proposed for microscale temperature measurements [12, 13], such as microfabricated thermocouples and resistance temperature detectors (RTD), infrared thermography, molecular tagging thermometry (MTT), laser induced fluorescence thermometry, thermochromic liquid crystals (TLCs), micro-Raman thermometry, and thermoreflectance. Among these techniques, TLCs, molecular tagging thermometry and laser induced fluorescence methods are the only ones amenable to non-intrusive, whole-field measurements inside a liquid.

Suspensions of encapsulated TLCs have been used to make transient temperature measurements in liquid droplets [14, 15]. These suspensions have also been used to make simultaneous velocity and temperature measurements [16, 17] by employing μPIV methods. The spatial resolution of TLCs is ~1 μm for surface temperature measurements, while it is of the order of 10 μm – 150 μm for measurements made inside a liquid, depending on the size of the particles. Sakakibara and Adrian [18] measured Rayleigh-Benard convection using two-color laser-induced fluorescence with an accuracy of ±0.17ºC. Hu et al. [19] conducted a detailed analysis of the temperature sensitivity of the molecular tagging thermometry method and claimed the error to be less than ±0.02ºC with a maximum temperature range of 2ºC over the entire field of view. It was observed that the error in temperature measurement had a quadratic dependence on the temperature range. All the three methods used a laser light sheet, the thickness of which was generally less than the depth of focus of the camera. In the

case of microscale measurements, volume-illumination is commonly used, and this would complicate the measurements further.

More recently, it was recognized that the Brownian motion of sub-micron sized particles, used to seed the liquid in μPIV measurements, can also be used to make temperature measurements. For small seed particles (< 1 μm diameter) in low speed flows (< 10 μm/s), the Brownian motion was significant enough to introduce errors in μPIV velocity measurements. The random movement of particles added to the uncertainty in locating the peak center. This undesirable error was substantially minimized through ensemble-averaging over multiple images, which had the effect of causing a width-wise spreading of the correlation peak [20]. Olsen and Adrian [21] performed a theoretical study on the effect of Brownian motion on the μPIV correlation signal peak and derived a function quantifying the increase in its width. This width-wise broadening of the correlation function was used to calculate the fluid temperature by Hohreiter et al. [1] with an experimental uncertainty of ±3°C.

Particle tracking [22-25] is a commonly used method to measure the displacements of particles and study Brownian motion. This method has also been adapted for obtaining microscale temperature measurements. Park et al. [26] used Optical Serial Sectioning Microscopy (OSSM) to measure Brownian particle displacements in all three dimensions and deduced temperature information with uncertainties of 5.54%, 4.26% and 3.19% for 1D, 2D and 3D cases, respectively. Kihm et al. [27] used 3D Ratiometric Total Internal Reflection Fluorescence Microscopy (3D R-TIRFM) to measure Brownian displacements near the wall and calculate the hindered diffusion constant of 200-nm particles along lateral and normal directions to the wall. The evanescent wave field generated from the total internal reflection illuminated only the particles which are a few hundred nanometers away from the wall. The experimental results showed good agreement with theory in the lateral direction but showed discrepancies in the normal direction; this was attributed to possible electrostatic and electro-osmotic interactions with the glass wall.

In the present study, the authors advance the work of Hohreiter et al. [1]. Three different methods are used to analyze sets of experimental images to obtain temperatures. The results are compared and the

advantages and disadvantages of each method identified. In the first method – Particle Image Velocimetry-based Thermometry (PIVT) technique – the peak-width expansion of the correlation functions is used to measure the Brownian displacement, which in turn yields temperature information. In the second method – Particle Tracking Thermometry (PTT) – each particle is tracked to obtain individual displacements. In the third method – Low Image Density (LID) PIV – cross-correlation analysis is conducted only in regions where particles are present, to obtain individual displacements for each particle. The PIVT technique is modified to simultaneously measure the velocity and temperature of a moving fluid. The effect of velocity gradients on the correlation function is accounted for and subtracted from the total broadening measured in order to separate the Brownian motion information, which is then used to determine the temperature of the fluid.

2. THEORETICAL MODEL

Stationary Fluid

As described in Hohreiter et al. [1], the idea of PIV-based thermometry is based on the theory of Brownian motion. The expression

$$D = \frac{kT}{3\pi\mu d_p} \tag{1}$$

defines the diffusivity D of particles with diameter d_p immersed in a liquid with absolute viscosity μ and temperature T; with k being Boltzmann's constant. Further, the mean square of the expected distance traversed by a particle with diffusivity D, within time Δt, is given by the expression

$$\left\langle s^2 \right\rangle = 2D\Delta t \tag{2}$$

Combining Equations (1) and (2) it can be seen that with all other variables held constant, the mean square displacement $\langle s^2 \rangle$ depends only on temperature as given by the relationship, $\langle s^2 \rangle \alpha\ T/\mu$, since absolute viscosity μ is a strong function of temperature. For a gas, increasing the temperature increases the absolute viscosity, which in turn might increase or decrease the value of T/μ depending on the fluid. For a liquid, increasing the temperature decreases the absolute viscosity, hence always increasing the value of T/μ.

Before the method can be developed further, the precise effect of Brownian motion on the spatial cross-correlation function must be understood. In a typical PIV experiment, two snapshots of the flow field are obtained at times t_1 and $t_2 = t_1 + \Delta t$. If these two images are denoted $I_1(X)$ and $I_2(X)$, then the cross-correlation function can be obtained using the convolution integral [28]:

$$R(S) = \int I_1(X) I_2(X+s) dX \tag{3}$$

$R(S)$ can be decomposed into three components as

$$R(S) = R_C(s) + R_F(s) + R_D(s) \tag{4}$$

where $R_C(s)$ is the convolution of the intensities of the two images and is a function of s with its diameter equal to the particle diameter, $R_F(s)$ is the fluctuating noise component, and $R_D(s)$ is the displacement component of the correlation function and gives the distance traveled by the particle during time Δt. Hence $R_D(s)$ is the component of the correlation function which contains the velocity information.

The displacement and the width of the correlation function depend on the probability function $f(x', t_2; x, t_1 | u(x), T)$ where f denotes the probability for a particle initially at (x, t_1) to move into the volume $(x', x' + dx)$ at t_2 for a known velocity field $u(x)$ and temperature T. In the absence of Brownian motion, $\Delta x = u(x, t_1)\Delta t$ is the displacement undergone by a particle at (x, t_1). Since for a given velocity field there can only be one final location for the particle, the probability function f becomes the delta function,

$$f(x', t_2; x, t_1 | u(x), T) = \delta(x' - x - \Delta x) \tag{5}$$

However, in the presence of Brownian motion, an exact value of displacement Δx cannot be defined and, as a result, f is no longer a delta function. Instead, f is now a probability distribution function centered at $x' = x + \Delta x$ and its shape is defined by the space-time correlation for Brownian motion defined by Chandrasekhar [29, 30].

$$f(x', t_2; x, t_1 | u(x), T) = (4\pi D \Delta t)^{-3/2} \times \exp\left[-(x' - x - \Delta x)^2 / (4 D \Delta t) \right] \tag{6}$$

This change in f due to Brownian motion has the effect of broadening the correlation function and reducing its height. The increase in the width of the correlation contains the information that yields temperature. This effect

is demonstrated in Figure 1, which shows the correlation functions with and without Brownian motion computed from experimental images.

Olsen and Adrian [21] derived analytical expressions to define the shape and height of the correlation function in the presence of Brownian motion for light-sheet PIV and volume-illumination PIV. For both cases the correlation function assumes a Gaussian shape and its center locates the mean particle displacement. In light-sheet PIV, the field of view of the camera can be set to be greater than the laser-sheet thickness so that all the particles in the image have the same diameter and peak intensity. The characteristics of the imaging optics play an important role in defining the relationship between the actual cross-section of the particle and that of its image [31]. Given a diffraction-limited lens, the image of a particle would be the convolution of the geometric image of the particle and the point response function of the imaging system. The point response function is an Airy function with diameter given by

$$d_S = 2.44(1+M)f^{\#}\lambda \tag{7}$$

where M is the magnification of the lens, $f^{\#}$ is the f-number of the lens, and λ is the wavelength of the light used to image the particles. Adrian and Yao [32] found that the Airy function as well as the particle image can be approximated by a Gaussian function, in which case the particle image diameter can be expressed by the formula,

$$d_e = (M^2 d_p^2 + d_s^2)^{1/2} \tag{8}$$

where, d_p is the particle diameter and M is the magnification of the lens used.

In volume-illumination PIV (for example, μPIV) the particle images are more complex. Since the entire channel is illuminated, all the particles along the optical axis of the camera would contribute to the resulting image. The particles closer to the focal plane form a sharp image while the particles away from the focal plane form a dim and blurry image. Olsen and Adrian [33] proposed that the particle image diameter in μPIV can be approximated as

$$d_e = (M^2 d_p^2 + d_s^2 + d_Z^2)^{1/2} \tag{9}$$

where

$$d_z = MzD_a/(x_0 + z) \tag{10}$$

and D_a is the aperture diameter of the microscope objective, z is the distance of the particle away from the focal plane, and x_0 is the object distance.

From an analysis of cross-correlation PIV, Olsen and Adrian [21] found that for light-sheet PIV, the width of the correlation peak, s_0, taken as the diameter of the Gaussian function measured at a height of $1/e$ times the peak value, can be expressed as

$$s_{o,a} = \sqrt{2d_e^2 / \beta^2} \tag{11}$$

in the absence of Brownian motion. When Brownian motion is present, the peak-width $s_{o,c}$, can be expressed as

$$s_{o,c} = \sqrt{2(d_e^2 + 8M^2\beta^2 D\Delta t)/\beta^2} \tag{12}$$

Equation (12) reduces to Equation (11) when Brownian motion ($D\Delta t$) is considered to be zero. The constant β is a parameter arising from approximating the Airy function to a Gaussian function and was found to be $\beta^2 = 3.67$ [32].

For the case of volume illumination, Equations (11) and (12) still hold, except that the term for particle image diameter, d_e must be replaced by the integral over the depth of the device. The cumbersome calculation of the integral term for d_e can be avoided by manipulation of Equations (11) and (12). Squaring Equation (11) and subtracting it from the square of Equation (12) gives the equation

$$\left\langle \Delta s_{BM}^2 \right\rangle = \frac{s_{o,c}^2 - s_{o,a}^2}{8M^2} = \frac{2k\Delta t}{3\pi d_p} \cdot \frac{T}{\mu} \tag{13}$$

which can be directly used to calculate temperature.

Parabolic Flow

In the presence of a non-uniform velocity field, there can be a velocity gradient across the interrogation window causing deformation of the correlation function. In the case of a Poiseuille flow, the velocity gradient itself is non-uniform across the channel. As a result, the probability distribution function f has a Brownian-motion component and a velocity-distribution component. For simple flows, if the velocity profile

is known, the probability distribution of velocities and the resulting broadening of the cross-correlation function can be computed using Monte Carlo simulation. This predicted peak-width increase (Δs^2_{vel}) can be subtracted from the total broadening measured (Δs^2_{Total}) to obtain the broadening due to Brownian motion alone (Δs^2_{BM}) as shown in Equation (14). In this analysis, a steady flow is assumed.

$$\Delta s_{BM}^2 = \Delta s_{Total}^2 - \Delta s_{Vel}^2 \tag{14}$$

The feasibility of this method is illustrated with the help of a numerical experiment as explained below. Figure 2 (a) shows the velocity profile across the channel and the error bars show the range of velocities present in each interrogation window at different radial locations. A uniform Brownian motion (temperature profile) is assumed across the channel. Figure 2 (b) shows the broadening in the cross-correlation function for different amounts of Brownian motion. The x-axis is the peak-width increase (in pixels) and the y-axis is the radial position across the channel. It can be seen that the peak-width increase is greatest near the walls where the maximum velocity gradient is present. In the absence of Brownian motion the increase in peak-width is due only to the velocity gradients present. As the amount of Brownian motion increases the curves become flatter. The peak-width increase due to Brownian motion alone can be obtained by subtracting the peak-width increase caused due to the velocity gradient. Figure 2 (c) shows this subtracted value. It can be seen that Brownian motion information can be obtained by subtracting the velocity gradient information.

Prior knowledge of the velocity field is required for the use of this method. In practice, this can be achieved by measuring the velocity field first and using that information to measure the temperature field. Since the velocity information is uncoupled from the temperature information, this does not pose a problem.

3. EXPERIMENTAL SETUP

To investigate the PIVT method, different test setups were devised for the stationary fluid and the parabolic flow cases. Both the experiments were conducted in a standard μPIV setup, shown in Figure 3, which consists of an upright Nikon Eclipse (ME600) microscope and an interline transfer Charge Coupled Device (CCD) camera (Roper Scientific Photometrics, CoolSNAP HQ). A Nikon mercury-arc lamp was used

as the illumination source. Metamorph imaging software was used to control the devices and acquire images. Fluorescent polymer microspheres (Duke Scientific Co.) of 0.69 μm diameter were used to seed the fluid. These particles absorb green light ($\lambda \sim 542$ nm) and emit red light ($\lambda \sim 612$ nm). The microspheres were polystyrene particles with a density of 1.05 g/cm^3.

The test piece used for both the stationary fluid and the parabolic flow experiments is shown in Figure 4. The stationary fluid experiments were conducted in a 400 μm square glass microchannel (Vitrocom, Inc.) submerged in a well machined into an aluminum block. The glass channel was filled with the particle solution, sealed on both sides and placed in the well which was then filled with deionized (DI) water and sealed on top with an acrylic plate. For the parabolic flow case, a circular Fluorinated Ethylene Propylene (FEP) tube of 200 μm diameter (Upchurch Scientific, Inc.) was used for the experiments. The matching refractive indices of water and FEP ensure that the particle images are not distorted due to the curvature of the tube. A gravity-induced flow was set up to achieve a steady velocity. The measurement region was approximately 100 tube diameters away from the entrance of the bath to locate it beyond the thermal development region.

The temperature of the DI water surrounding the well was used as the reference temperature and was measured using a thermocouple. The aluminum block was heated using a thermofoil resistance heater (Minco Products, Inc.) and was enclosed in an insulating material. Measurements were taken at seven different temperatures ranging from 20°C to 80°C. At each temperature, measurements were obtained after sufficient time had elapsed, allowing the setup to reach thermal equilibrium. For the stationary fluid experiment 700 images were taken at each temperature, while for the parabolic flow experiment, 1875 images were obtained at each temperature to obtain statistically valid results. A particle volume fraction of 0.001 was used in both the experiments.

4. RESULTS AND DISCUSSION

The PIV-based thermometry (PIVT) and low image density PIV (LID PIV) methods were implemented using EDPIV [34, 35] (a PIV code specially adapted for microscale flows, developed by Dr. Lichuan Gui),

which was programmed to provide evaluation functions for each interrogation window averaged over the entire set of images. Background subtraction is performed on all the images to reduce noise due to non-uniform illumination. No other advanced image deformation algorithms were employed.

4.1 Stationary Fluid Experiments

The temperatures measured using PIV thermometry are compared to the results obtained using the PTT and LID PIV thermometry methods. All three methods of analysis were applied to the same set of images to allow for a direct comparison.

μPIV-Based Thermometry (PIVT)

The analysis method for the PIVT method is shown in Figure 5. The image is split into smaller windows of a specified size. The correlation functions and velocity vectors are evaluated in each window using the software. An interrogation window with 128*128 pixels was used to ensure the presence of particles in every window. Since the particles were suspended in a stationary fluid, velocity vectors were not of interest. The evaluation functions were processed in MATLAB® (The MathWorks, Natick, MA). The evaluation functions were averaged over the entire image and a 2D Gaussian fitting program was used to measure the peak-width of the evaluation function. In order to fully characterize a 2D Gaussian function, given by the equation

$$G(x,y) = A\exp(\frac{-(x-x_0)^2}{2\sigma_x^2})\cdot\exp(\frac{-(y-y_0)^2}{2\sigma_y^2}), \qquad (15)$$

five parameters must be defined: the peak height A, the coordinates locating the peak center x_0 and y_0 and standard deviation values in the x and y directions, σ_x and σ_y. If σ_x is equal to σ_y then the Gaussian function has a circular cross section; otherwise, it would have an elliptical cross section. This standard deviation is related to the peak-width as $\Delta s^2 = 8\cdot\sigma^2$, and contains Brownian motion information. In this case since the images were taken far from the walls of the channel, the Brownian motion should be identical in all directions resulting in a circular Gaussian function.

The temperatures were calculated using Equation (13) and are plotted in Figure 5 The average difference between the predicted and measured temperatures was ±2.1°C. The advantage of the PIVT method is that a high concentration of particles can be used as long as the particles do not interact with each other, yielding the highest possible number of data points. Also, while measuring temperature in the presence of a flow field, this method would be much less cumbersome than a particle tracking technique. The main disadvantage of this method is the error introduced in the measured shape of the correlation function due to uneven illumination and background noise in the image. Standardized image processing techniques were used to eliminate this noise in the present work. Advanced algorithms such as Central Difference Image Correction (CDIC) and Continuous Window Shifting (CWS) cannot be used as they distort the shape of the correlation function.

Particle Tracking Thermometry (PTT)

Particle tracking thermometry is performed in two steps – particle identification and particle tracking. The technique is illustrated in Figure 6. Each image is read into MATLAB where all the particles in the image are identified based on a given threshold intensity. A Gaussian function is then fit on to each particle to locate the center of the particle. The information of all the particle locations is stored and a tracking algorithm is used to measure individual displacements. To track the particles, the program chooses each particle and searches for it in the second image in an area surrounding its initial location. Once a match is found, the difference between the coordinates of the two locations gives the displacement.

Once all the particles are tracked, the standard deviation of the displacements directly gives the RMS Brownian displacement $\sqrt{\langle s^2 \rangle}$, from which temperature can be calculated using Equation (2). Assuming that the concentration of the solution is low enough to avoid any particle groups, the only error involved in the method is the uncertainty in locating the centers of the particles. Since for each particle displacement the Gaussian fitting function is used twice, the error involved in the measurement of each displacement is $\sqrt{2}$ times that for the peak location in PIV.

It must be noted that if there are two or more particles located very close to each other, the program will have an equal likelihood of choosing either of the particles as a match. Such erroneous displacements are denoted by the dotted arrows in Figure 6 (b). Thus, it is essential that the particle concentration be very low for this method. There may also be a few unmatched particles due to those that have migrated out of the depth of field or field of view. However, unlike in cross-correlation PIV, such particles are disregarded if the program is unable to find a match, with no deleterious effects. The results obtained are plotted in Figure 6 (c). The average difference between the predicted and measured temperature was ±2.6°C.

LID PIV Thermometry (LID PIVT)

This method combines the advantages of the cross-correlation PIV and the PTT methods, and is illustrated in Figure 7. The first step is to identify the particles in each image based on a given threshold intensity. Once this is done, instead of recording particle locations, PIV cross-correlation analysis is performed. In traditional PIV the entire image is broken down into uniformly-spaced smaller interrogation regions for analysis. In the LID PIV method, interrogation windows are formed and cross-correlation analysis done only at locations where particles are identified. Individual displacements for each particle are available from the analysis, from which the temperature can be deduced using Equation (2).

The main advantage of this method is that Gaussian fitting, a significant source of error, is employed only once to locate the displacement of the correlation peak as opposed to the two times needed in the PTT method. In addition, since displacements are used to calculate temperature, the particle image diameter and the background noise are not of concern. Also, advanced interrogation algorithms like CDIC and CWS may be applied.

The disadvantage of the method is that if more than one particle appears in an interrogation window, the resulting displacement is the mean of the displacements of all the particles in the window. Such erroneous displacements are denoted by dotted arrows in Figure 7 (b). Since the particles undergoing Brownian motion exhibit random behavior, even with a very low concentration, there is still a chance for a few particles to come close to each other. One possible solution would be to identify the interrogation windows with more than one

particle and disregard the corresponding displacement values. An alternate solution would be to use a correction factor to account for the decrease in peak-width measurement due to the particle groups present. It was observed that the interrogation windows with more than one particle typically contained 2 to 4 particles. Figure 8 (a) shows the percentage error in peak-width (*i.e.*, percentage decrease in the standard deviation of the Gaussian distribution of displacements) as a function of the percentage number of interrogation windows that have more than one particle. It can be seen that as the number of interrogation windows with multiple particles increases, the error in the peak-width measurement increases. The figure shows that for interrogation windows consisting of up to four particles each, the temperature measurement error would be less than 5% as long as the number of such interrogation windows is less than 10% of the total number of interrogation windows in the entire data set. In practice, it is difficult to theoretically predict the correction factor as the number of particles in each interrogation window will vary from image to image. Hence, to use this method, a calibration step is necessary to obtain the correction factor. For this experiment it was observed that with a correction factor of 1.15 the measured values show good agreement with the expected temperature values. These values are plotted in Figure 8 (b). With this correction factor, it was observed that the average difference between the predicted and measured temperatures was ±1.5°C.

4.2 Parabolic Flow Experiments

Since the Brownian motion along each coordinate axis is independent of the other axes, the diffusion in the x and y directions can be measured separately at each location. As a uniform temperature was applied across the channel, Brownian motion in the x and y directions should be uniform along the radial direction. Since the velocity gradient affects only the standard deviation in the x direction (σ_x), σ_y is a measure of Brownian motion alone and will be uniform across the channel. The σ_x contains both Brownian motion and velocity gradient information and varies according to the gradients present in each window.

The peak-width increase in the y direction was measured for different temperatures and plotted as a function of the radial location in Figure 9 (a). The peak-width increase $\sqrt{\langle s^2 \rangle}$, given by Equation (13), is the

square root of the difference between the squares of the cross correlation peak-width and the auto correlation peak-width. The peak-width increase was measured using an interrogation window of size 128*128 pix^2. It can be seen that the Brownian motion is uniform across the channel and that it increases as the temperature increases. The slight variation in the profiles is due to insufficient data points in the window to obtain a statistically averaged result.

Figure 9 (b) shows the peak-width increase measured in the x direction for different temperatures. It can be seen that the experimental profiles for peak-width increase match well with the theoretical profiles shown in Figure 2. The peak broadening near the walls is larger due to the high velocity gradients present in this region.

The peak-width increase in the x direction contains both Brownian motion and velocity gradient information. The effect due to the velocity gradient was calculated using the measured velocity profile and subtracted for temperatures 22.8°C and 55.0°C. Figure 10 (a) shows the total peak-width increase and the corrected peak-width increase plotted as a function of the radial location. It can be seen that after correction the profiles are quite uniform across the channel as expected. The corrected peak-width increase in the streamwise direction was observed to be larger than the peak-width increase in the y direction. This is attributed to minor fluctuations in the flow (less than 2% of the mean flow) due to vibrations near the experimental set-up. The peak-width increase in the streamwise direction and the cross-streamwise direction near the center of the channel should be the same due to the low shear present in that region. Hence, the difference between the peak-width increase in the streamwise and cross-streamwise directions at the center of the channel gives the peak-width increase due to these velocity fluctuations. It was observed that by subtracting this value from the peak-width increase, the profile matches with that in the cross-streamwise direction.

The temperature values obtained from the mean peak-width increase in the cross-streamwise direction and the corrected peak-width increase in the streamwise direction were plotted against the expected values in Figure 10 (b). The average difference between the measured and expected temperatures was found to be

±2.6ºC. The corrected peak-width increase in the x direction is larger than the peak-width increase in the y direction, indicating a different calibration constant in the x direction.

4.3 Experimental Uncertainty

The uncertainty involved in the measurement technique is evaluated using the single-sample method proposed by Kline and McClintock [36]. By conducting the standard analysis on Equation (13), we obtain the expression,

$$\omega_T = \pm T \left\{ \left(\frac{\omega_{d_P}}{d_P} \right)^2 + \left(2\frac{\omega_{\Delta s}}{\Delta s} \right)^2 + \left(\frac{\omega_{\Delta t}}{\Delta t} \right)^2 + \left(\frac{\omega_{\mu}}{\mu} \right)^2 + \left(2\frac{\omega_M}{M} \right)^2 \right\}^{1/2} \qquad (16)$$

where ω is the error in the measurement of the quantity denoted by subscript. Since the viscosity of the fluid is a known quantity that depends on temperature, the uncertainty in its value is directly related to the uncertainty in temperature. Hence, by treating viscosity as a function of temperature[37] we obtain the relation,

$$\omega_T = \pm T \left\{ \frac{\left[\left(\frac{\omega_{d_P}}{d_P} \right)^2 + \left(2\frac{\omega_{\Delta s}}{\Delta s} \right)^2 + \left(\frac{\omega_{\Delta t}}{\Delta t} \right)^2 + \left(2\frac{\omega_M}{M} \right)^2 \right]^{1/2}}{\left[1 - \left(\frac{T}{\mu}\frac{d\mu}{dT} \right)^2 \right]} \right\} \qquad (17)$$

For the current experimental setup the error introduced due to the uncertainty in the magnification (ω_M) and the time delay between particle images ($\omega_{\Delta t}$) can be assumed to be negligible. The variation in the size of the fluorescent particles is given by the manufacturer as 3% of the mean diameter. The uncertainty in the estimation of the peak-width ($\omega_{\Delta S}$) was estimated by measuring the variation in the peak-width value for the entire image set. Thus $\omega_{\Delta S}$ for the current experimental parameters was experimentally found to be 0.03 pixels. By substituting these values in Equation (17), the maximum uncertainty in the measurement technique for the temperature range 20ºC to 80 ºC was found to be ±0.5ºC. It can be seen that this value is less than actual deviation observed in the experimental results. This is attributed to the additional uncertainty imposed by the thermocouple measurements which is estimated to be ±1.0ºC.

4.4 Design Considerations for Future Experiments

The sensitivity of the experimental technique can be improved by appropriately choosing the experimental parameters. Figure 11 (a) shows the peak-width increase in pixels due to Brownian motion for temperatures ranging from 20ºC to 80ºC. By using a higher magnification objective, the Brownian displacement can be magnified, but this also results in a smaller field of view requiring more images to obtain the same signal to noise ratio. Similarly, smaller-sized particles exhibit greater amounts of Brownian motion while compromising the particle image quality. The time interval between particle images should be chosen such that the particles exhibit sufficient displacement while staying within the interrogation window.

For the case of particles in a flow, care should be taken so that the maximum particle displacement due to the flow is comparable to the RMS Brownian displacement. For a particular velocity of the fluid, the time difference between the images should be small enough such that the particles stay within the interrogation window but large enough to resolve the Brownian displacement of the particles. Let the time difference between the images be fixed such that the displacement of the particles due to the flow is 50 pixels between a pair of images. Then, for a given velocity of the fluid, the size of the particle is decided such that its rms Brownian displacement is 2 pixels in that time difference. This would give us the maximum size of the particle that can be used with a given velocity of the fluid, to obtain a resolvable amount of Brownian displacement. In other words, for a fixed particle size it gives the maximum velocity of the fluid that can be allowed. Figure 11 (b) shows the maximum allowable velocity of the fluid as a function of particle size for different magnifications. It can be seen that even with a 100X objective, the maximum velocity of the fluid allowable with a 0.3 μm particle is below 1 mm/s. As the size of the particle is decreased below the wavelength of light, it becomes harder to image the particle. Also, if the particle size is smaller than the diffraction-limited spot size for the objective, small displacements cannot be resolved leading to error in the measurements.

5. CONCLUSIONS

PIV thermometry has been developed as a non-intrusive whole-field diagnostic tool suitable for making simultaneous microscale measurements of temperature and velocity in steady flows. The same experimental setup and images used for μPIV measurements can be used to obtain temperature information.

The Low Image Density (LID) PIV tracking method was found to perform better than cross-correlation PIV and Single Particle Tracking Thermometry (SPTT) methods for measuring temperatures based on Brownian motion of particles in a stationary well of liquid. However it should be noted that the concentration of particles should be very low for the LID PIV method to produce accurate results. Also, its performance could be improved by introducing the capability in the program to locate and disregard particle groups. SPTT was found to be the slowest and least accurate method of the three. In the case of cross correlation PIV, good image processing techniques should be defined to correct irregular illumination and remove background noise, in order to standardize the method.

The PIV thermometry method was tested in the presence of a flow. The velocity vectors measured using μPIV were used to calculate the peak broadening induced due to the velocity gradients present in each interrogation window. This was used to obtain the peak-width increase due to Brownian motion alone, from which temperature was measured. The average difference between the measured and predicted temperatures was found to be ±2.6ºC. The accuracy of the method can be improved by using a larger image set to obtain statistically averaged results. The measurement in the x direction was found to have a bias which might be due to noise in the velocity. This bias is being analyzed as a part of the ongoing work in this project.

Acknowledgement

Support for this work from the Indiana 21st Century Research and Technology Fund is gratefully acknowledged.

REFERENCES

1. Hohreiter, V., Wereley, S.T., Olsen, M.G., and Chung, J.N., 2002, "Cross-correlation analysis for temperature measurement," *Measurement Science & Technology*, **13**(7), pp. 1072-1078.
2. Anderson, R.C., Bogdan, G.J., Barniv, Z., Dawes, T.D., Winkler, J., and Roy, K., 1997, "Microfluidic biochemical analysis system", in *Transducers 97 - 1997 International Conference on Solid-State Sensors and Actuators, Digest of Technical Papers, Vols 1 and 2*. p. 477-480.
3. Chiem, N., Colyer, C., and Harrison, D.J., 1997, "Microfluidic systems for clinical diagnostics", in *Transducers 97 - 1997 International Conference on Solid-State Sensors and Actuators, Digest of Technical Papers, Vols 1 and 2*. p. 183-186.
4. Bisson, C., Campbell, J., Cheadle, R., Chomiak, M., Lee, J., Miller, C., Milley, C., Pialis, P., Shaw, S., Weis, W., and Widrig, C., 1998, "A microanalytical device for the assessment of coagulation parameters in whole blood," *The Solid-State Sensor and Actuator Workshop*. Hilton head, SC.
5. Manz, A., Graber, N., and Widmer, H.M., 1990, "Miniaturized total chemical-analysis systems - a novel concept for chemical sensing," *Sensors and Actuators B-Chemical*, **1**(1-6), pp. 244-248.
6. Service, R., 1998, "A biomolecule building block from vents " *Science*, **282**(5387), pp. 243-243.
7. Burns, J.R. and Ramshaw, C., 1999, "Development of a microreactor for chemical production," *Chemical Engineering Research & Design*, **77**(A3), pp. 206-211.
8. Ehrfeld, W., Hessel, V., and Lehr, H., 1998, "Microreactors for chemical synthesis and biotechnology - Current developments and future applications", in *Microsystem Technology in Chemistry and Life Science*. p. 233-252.
9. DeWitt, S., Boyce-Jacino, M., Lin, C., Kugelmass, S., Schnerr, G., and Swenson, R., 2000, "Microfluidic chips for pharmacogenomics and chemistry," *Abstracts of Papers of the American Chemical Society*, **219**, pp. U767-U767.
10. Garimella, S.V., 2006, "Advances in mesoscale thermal management technologies for microelectronics," *Microelectronics Journal*, **37**(11), pp. 1165-1185.
11. Garimella, S.V., Singhal, V., and Liu, D., 2006, "On-chip thermal management with microchannel heat sinks and integrated micropumps," *Proceedings of the Ieee*, **94**(8), pp. 1534-1548.
12. Childs, P.R.N., Greenwood, J.R., and Long, C.A., 2000, "Review of temperature measurement," *Review of Scientific Instruments*, **71**(8), pp. 2959-2978.
13. Yoo, J.Y., 2006, "Recent studies on fluid flow and heat transfer in thermal microdevices," *Nanoscale and Microscale Thermophysical Engineering*, **10**(1), pp. 67-81.
14. Richards, C.D. and Richards, R.F., 1998, "Transient temperature measurements in a convectively cooled droplet," *Experiments in Fluids*, **25**(5-6), pp. 392-400.
15. Nozaki, T., Mochizuki, T., Kaji, N., and Mori, Y.H., 1995, "Application of liquid-crystal thermometry to drop temperature measurements," *Experiments in Fluids*, **18**(3), pp. 137-144.
16. Fujisawa, N., Funatani, S., and Katoh, N., 2005, "Scanning liquid-crystal thermometry and stereo velocimetry for simultaneous three-dimensional measurement of temperature and velocity field in a turbulent Rayleigh-Bernard convection," *Experiments in Fluids*, **38**(3), pp. 291-303.
17. Funatani, S. and Fujisawa, N., 2002, "Simultaneous measurement of temperature and three velocity components in planar cross section by liquid-crystal thermometry combined with stereoscopic particle image velocimetry," *Measurement Science & Technology*, **13**(8), pp. 1197-1205.
18. Sakakibara, J. and Adrian, R.J., 2004, "Measurement of temperature field of a Rayleigh-Benard convection using two-color laser-induced fluorescence," *Experiments in Fluids*, **37**(3), pp. 331-340.
19. Hu, H. and Koochesfahani, M.M., 2003, "A novel technique for quantitative temperature mapping in liquid by measuring the lifetime of laser induced phosphorescence," *Journal of Visualization*, **6**(2), pp. 143-153.
20. Santiago, J.G., Wereley, S.T., Meinhart, C.D., Beebe, D.J., and Adrian, R.J., 1998, "A particle image velocimetry system for microfluidics," *Experiments in Fluids*, **25**(4), pp. 316-19.
21. Olsen, M.G. and Adrian, R.J., 2000, "Brownian motion and correlation in particle image velocimetry," *Optics and Laser Technology*, **32**(7-8), pp. 621-627.
22. Salmon, R., Robbins, C., and Forinash, K., 2002, "Brownian motion using video capture," *European Journal of Physics*, **23**(3), pp. 249-253.
23. Crocker, J.C., 1997, "Measurement of the hydrodynamic corrections to the Brownian motion of two colloidal spheres," *Journal of Chemical Physics*, **106**(7), pp. 2837-2840.
24. Crocker, J.C. and Grier, D.G., 1996, "Methods of digital video microscopy for colloidal studies," *Journal of Colloid and Interface Science*, **179**(1), pp. 298-310.

25. Nakroshis, P., Amoroso, M., Legere, J., and Smith, C., 2003, "Measuring Boltzmann's constant using video microscopy of Brownian motion," *American Journal of Physics*, **71**(6), pp. 568-573.
26. Park, J.S., Choi, C.K., and Kihm, K.D., 2005, "Temperature measurement for a nanoparticle suspension by detecting the Brownian motion using optical serial sectioning microscopy (OSSM)," *Measurement Science & Technology*, **16**(7), pp. 1418-1429.
27. Kihm, K.D., Banerjee, A., Choi, C.K., and Takagi, T., 2004, "Near-wall hindered Brownian diffusion of nanoparticles examined by three-dimensional ratiometric total internal reflection fluorescence microscopy (3-D R-TIRFM)," *Experiments in Fluids*, **37**(6), pp. 811-824.
28. Keane, R.D. and Adrian, R.J., 1992, "Theory of cross-correlation analysis of PIV images," *Applied Scientific Research*, **49**(3), pp. 191-215.
29. Chandrasekhar, S., 1941, "Statistical theory of stellar encounters," *Astrophysical Journal*, **94**(3), pp. 511-524.
30. Edwards, R.V., Angus, J.C., French, M.J., and Dunning, J.W., 1971, "Spectral Analysis of Signal from Laser Doppler Flowmeter - Time-Independent Systems," *Journal of Applied Physics*, **42**(2), pp. 837-850.
31. Adrian, R.J., 1991, "Particle-imaging techniques for experimental fluid-mechanics," *Annual Review of Fluid Mechanics*, **23**, pp. 261-304.
32. Adrian, R.J. and Yao, C.S., 1985, "Pulsed laser technique application to liquid and gaseous flows and the scattering power of seed materials," *Applied Optics*, **24**(1), pp. 44-52.
33. Olsen, M.G. and Adrian, R.J., 2000, "Out-of-focus effects on particle image visibility and correlation in microscopic particle image velocimetry," *Experiments in Fluids*, **29**, pp. S166-S174.
34. Gui, L. and Wereley, S.T., 2002, "A correlation-based continuous window-shift technique to reduce the peak-locking effect in digital PIV image evaluation," *Experiments in Fluids*, **32**(4), pp. 506-17.
35. Gui, L., Wereley, S.T., and Kim, Y.H., 2003, "Advances and applications of the digital mask technique in particle image velocimetry experiments," *Measurement Science & Technology*, **14**(10), pp. 1820-1828.
36. Kline, S.J. and McClintock, F.A., 1953, "Describing uncertainties in single-sample experiments," *Mechanical Engineering*, **75**(1), pp. 3-9.
37. Fox, R.W., McDonald, A.T., and Pritchard, P.J., Introduction to Fluid Mechanics. 6th ed. 2004, Hoboken, N.J.: Wiley. xii, 787 p.

LIST OF FIGURES

against measured temperatures. The average difference between the predicted and measured temperatures is ±1.5ºC.

Figure 9 (a) Peak-width increase in the y direction for different temperatures plotted as a function of radial location measured using an interrogation window of size 128*128 pix^2. (b) Total peak-width increase in the x direction for different temperatures plotted as a function of radial location measured using an interrogation window of size 128*128 pix^2.

Figure 10 (a) Total peak-width increase in the x direction and the corrected peak-width increase corresponding to the Brownian motion plotted as a function of radial location. (b) Temperatures determined using Brownian motion plotted against the thermocouple temperatures. The average difference between the expected and average temperatures was ±2.6ºC.

Figure 11 (a) The peak-width increase in pixels as a function of the magnification for the temperature range of 20ºC - 80ºC. (b) The maximum allowable velocity of the fluid as a function of the size of the particle for which the Brownian motion can still be resolved.

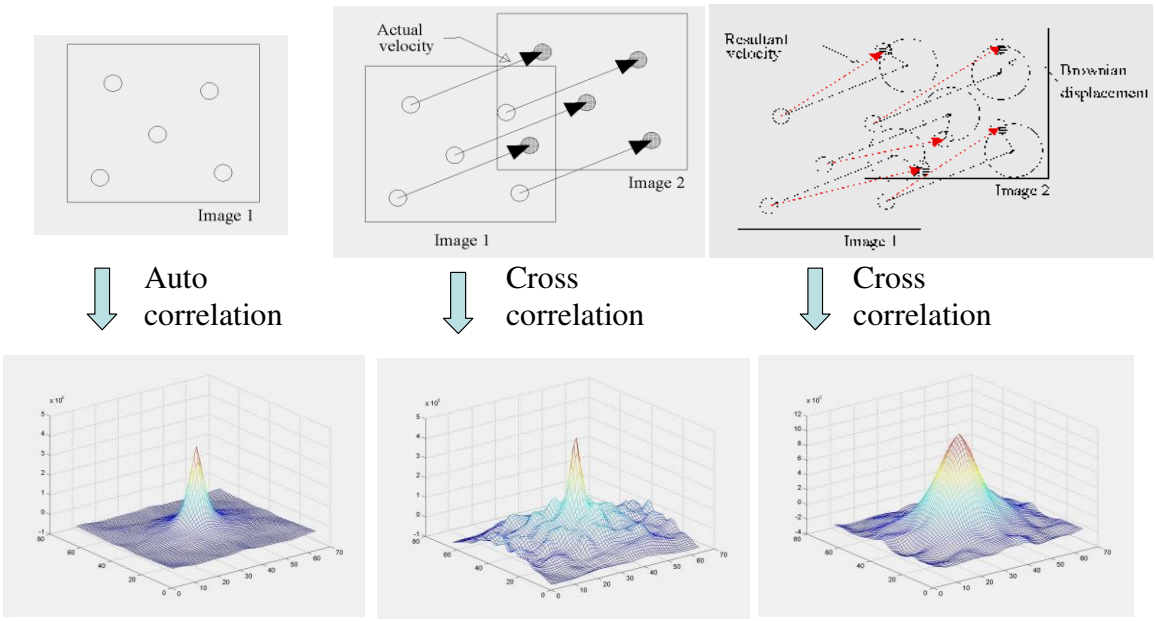

$$(a)\Delta s_{o,a} = \sqrt{2d_e^2/\beta^2} \qquad (b)\Delta s_{o,c} = \sqrt{2d_e^2/\beta^2} \qquad (c)\Delta s_{o,c} = \sqrt{2(d_e^2 + 8M^2\beta^2 D\Delta t)/\beta^2}$$

Figure 1 A comparison of the (a) auto-correlation, (b) cross-correlation function without any Brownian motion, and (c) cross-correlation function with Brownian motion.

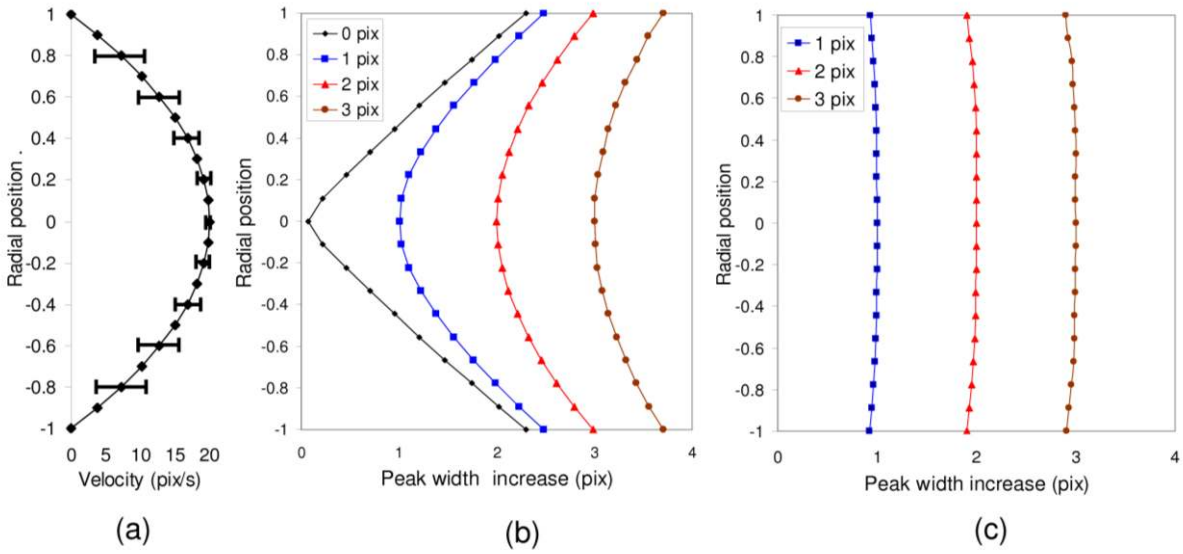

Figure 2 (a) Velocity in pixels as a function of radial position, (b) total peak-width increase due to the velocity field shown in (a) for varying amounts of Brownian motion, and (c) peak-width increase due to Brownian motion obtained by subtracting the velocity gradient effect.

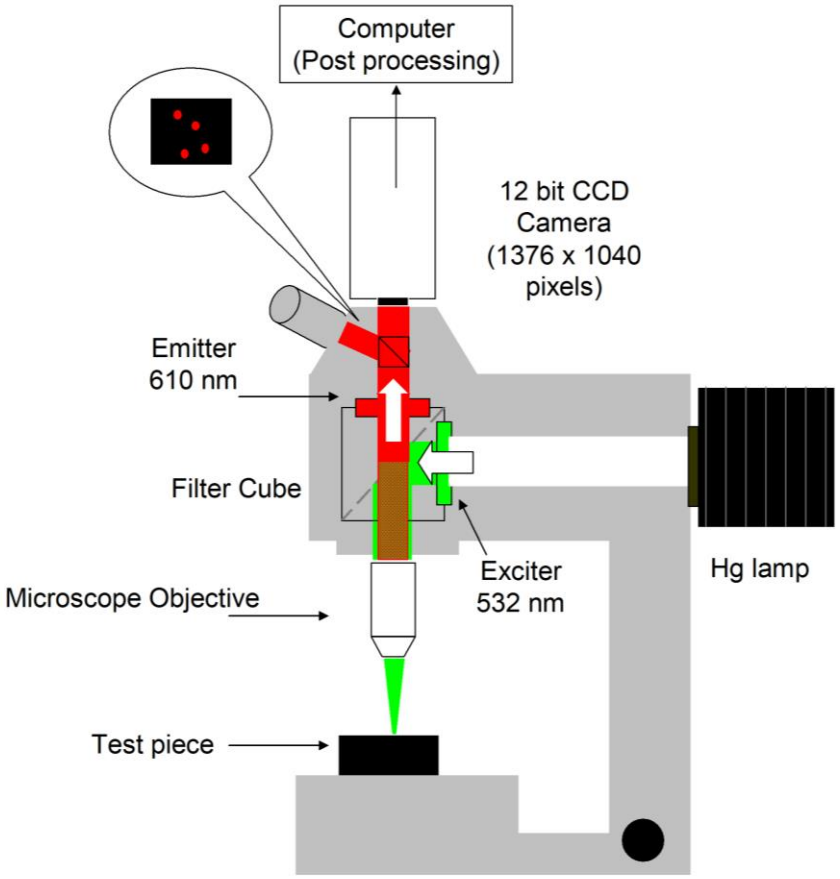

Figure 3 µPIV experimental setup.

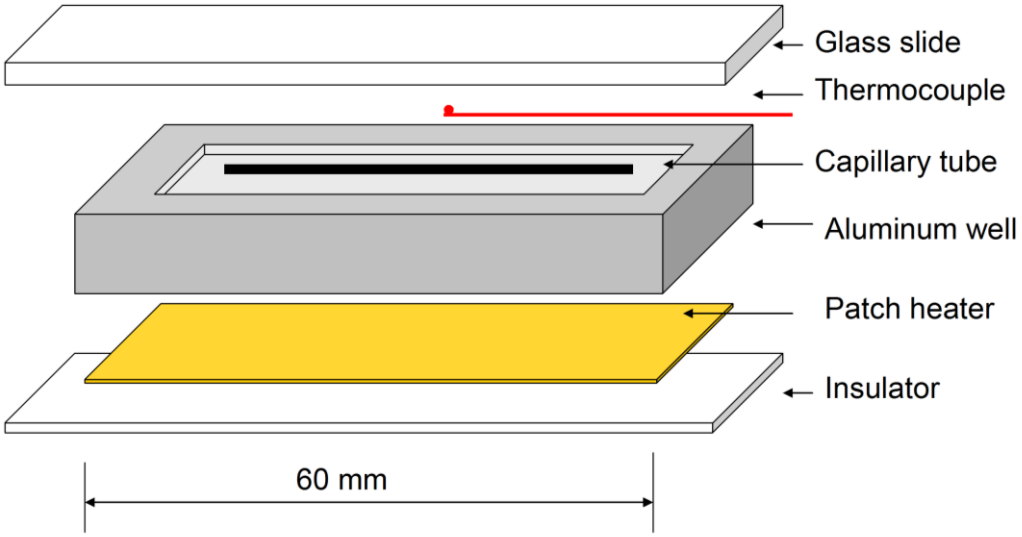

Figure 4 Experimental test piece for the stationary fluid experiments.

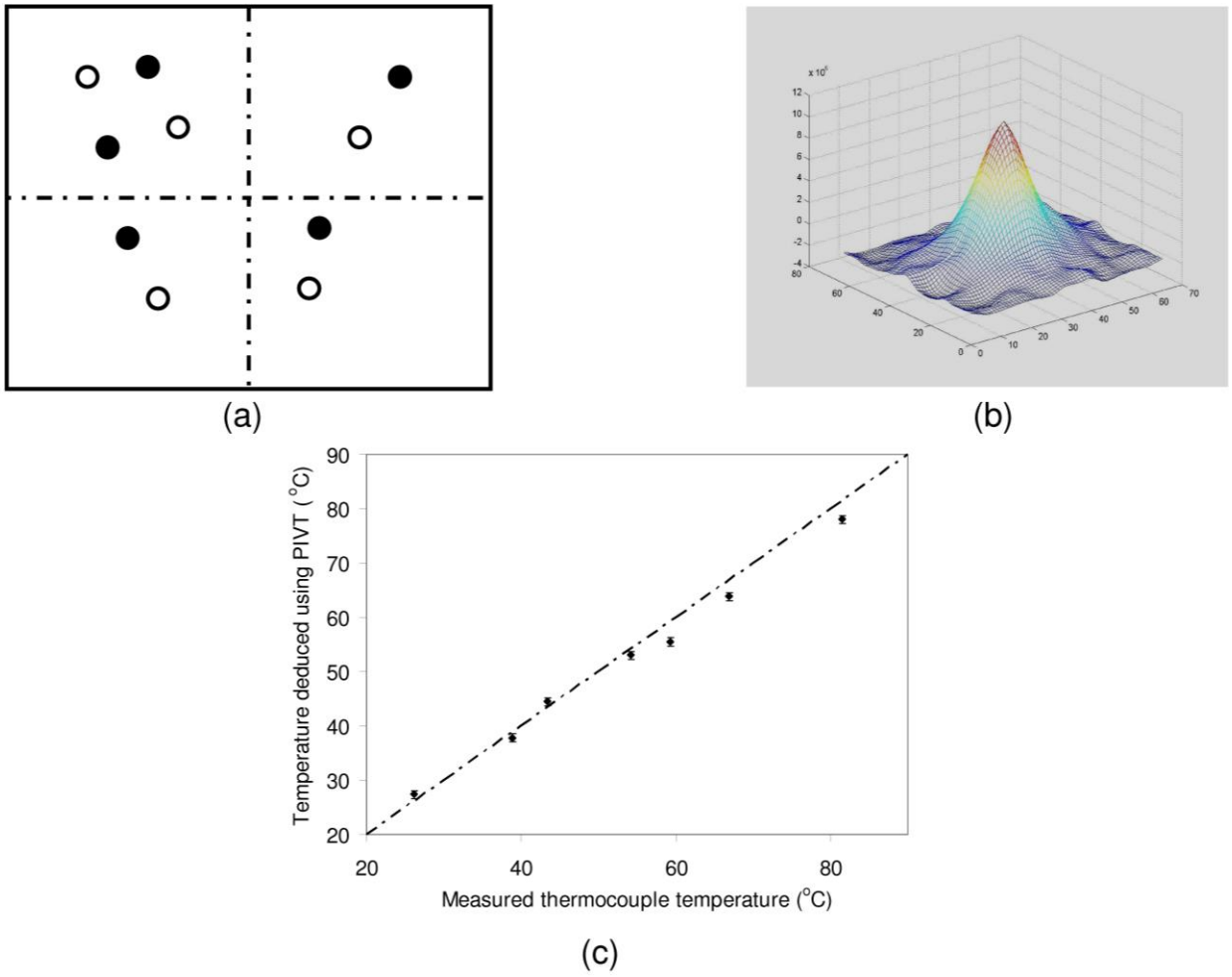

Figure 5 Illustration of the PIV thermometry technique: (a) image 1 (open circles) superimposed on image 2 (closed circles); (b) cross-correlation peak-width is used to obtain temperature measurements; and (c) temperatures deduced using the PIVT method plotted against measured temperatures. The average difference between the predicted and measured temperatures is ±2.1ºC.

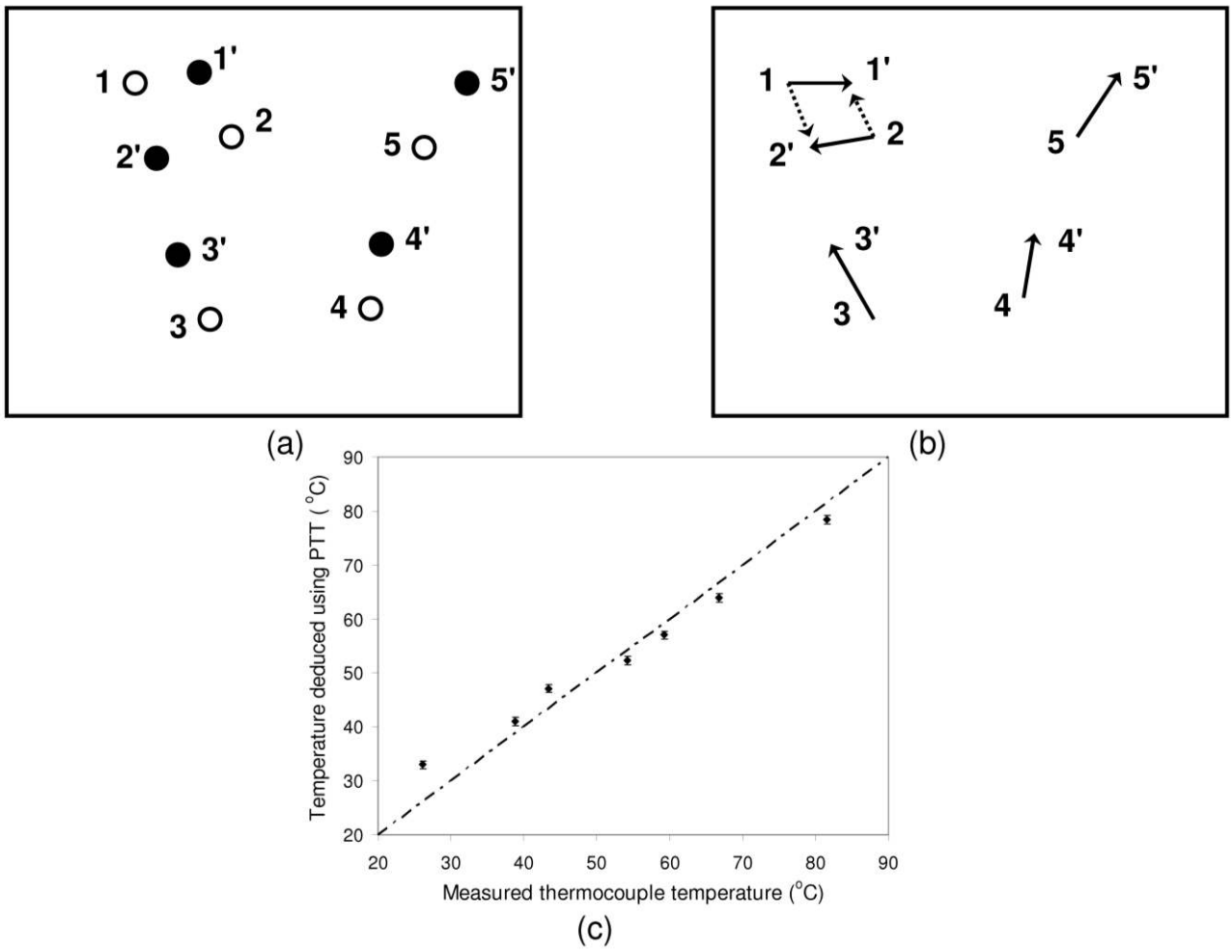

Figure 6 Illustration of the Particle Tracking Thermometry technique: (a) image 1 (open circles) superimposed on image 2 (closed circles); (b) particle locations identified in each image and displacements then calculated using probabilistic arguments; and (c) temperatures deduced using the PTT method plotted against measured temperatures. The average difference between the predicted and measured temperatures is ±2.6ºC.

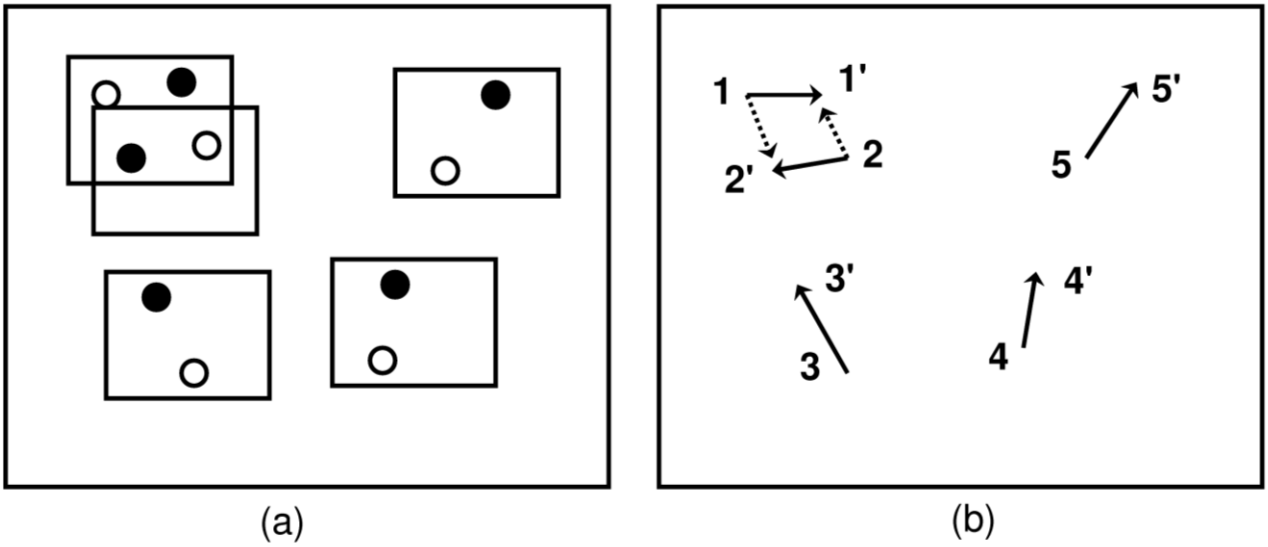

Figure 7 Illustration of the LID PIV technique: (a) image 1 (open circles) superimposed on image 2 (closed circles), amd (b) cross-correlation analysis to obtain displacement of each particle.

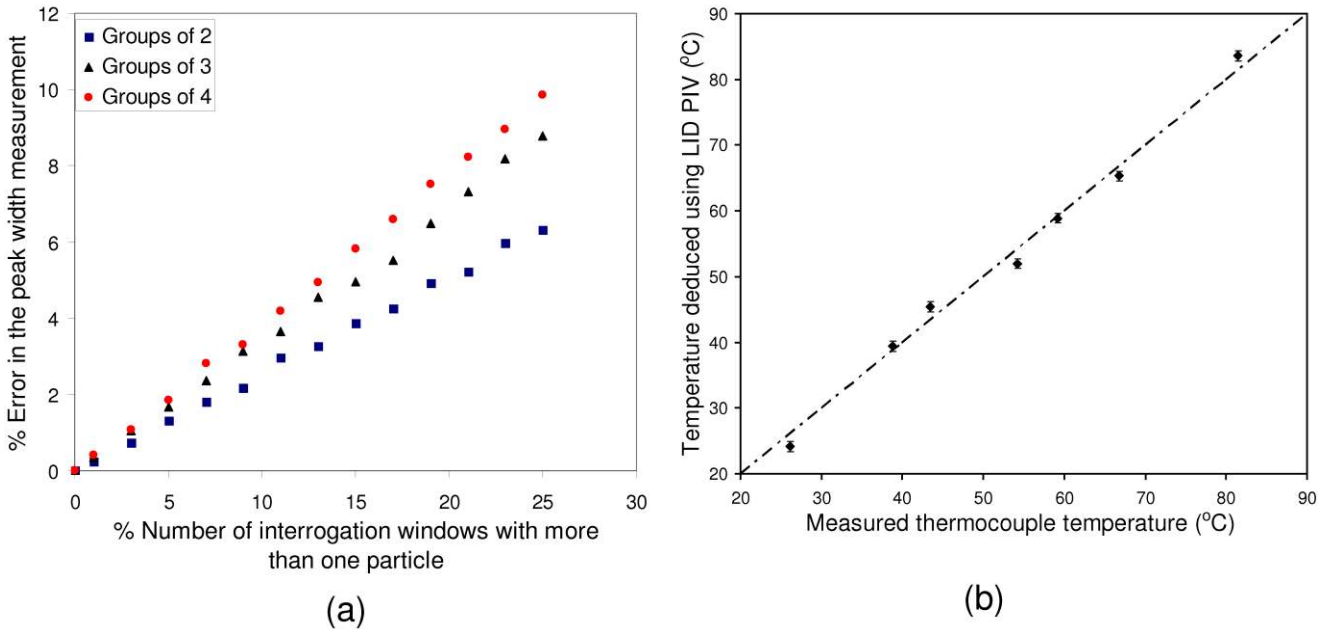

Figure 8 (a) Percentage error in the peak-width measurement introduced as the number of interrogation windows with multiple particles increases. (b) Temperatures deduced using the LID PIVT method plotted against measured temperatures. The average difference between the predicted and measured temperatures is ±1.5ºC.

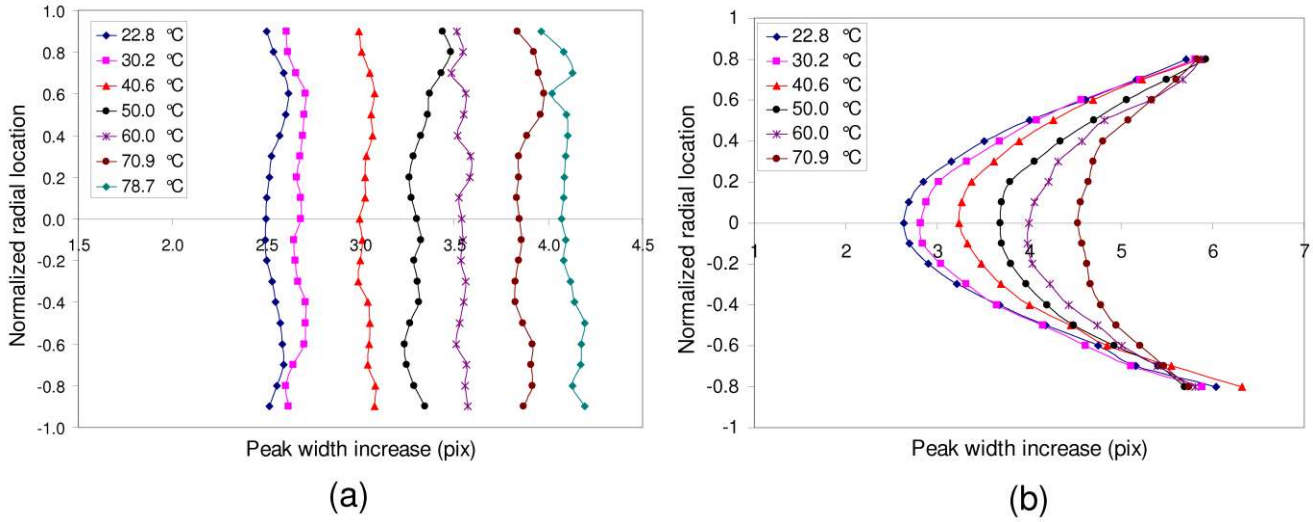

Figure 9 (a) Peak-width increase in the y direction for different temperatures plotted as a function of radial location measured using an interrogation window of size 128*128 pix^2. (b) Total peak-width increase in the x direction for different temperatures plotted as a function of radial location measured using an interrogation window of size 128*128 pix^2.

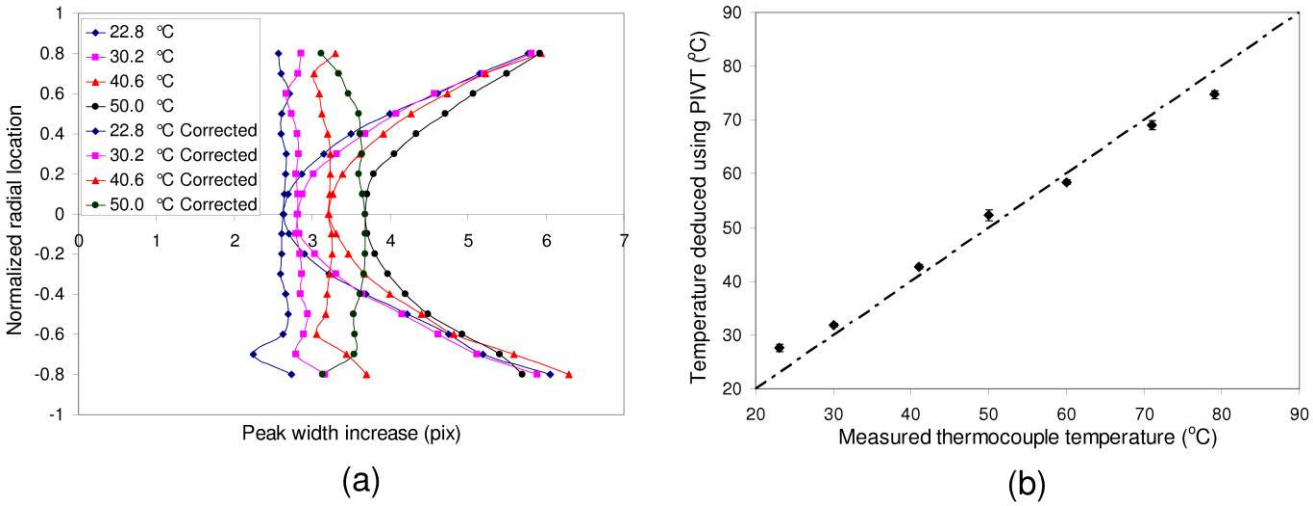

Figure 10 (a) Total peak-width increase in the x direction and the corrected peak-width increase corresponding to the Brownian motion plotted as a function of radial location. (b) Temperatures determined using Brownian motion plotted against the thermocouple temperatures. The average difference between the expected and average temperatures was ±2.6ºC.

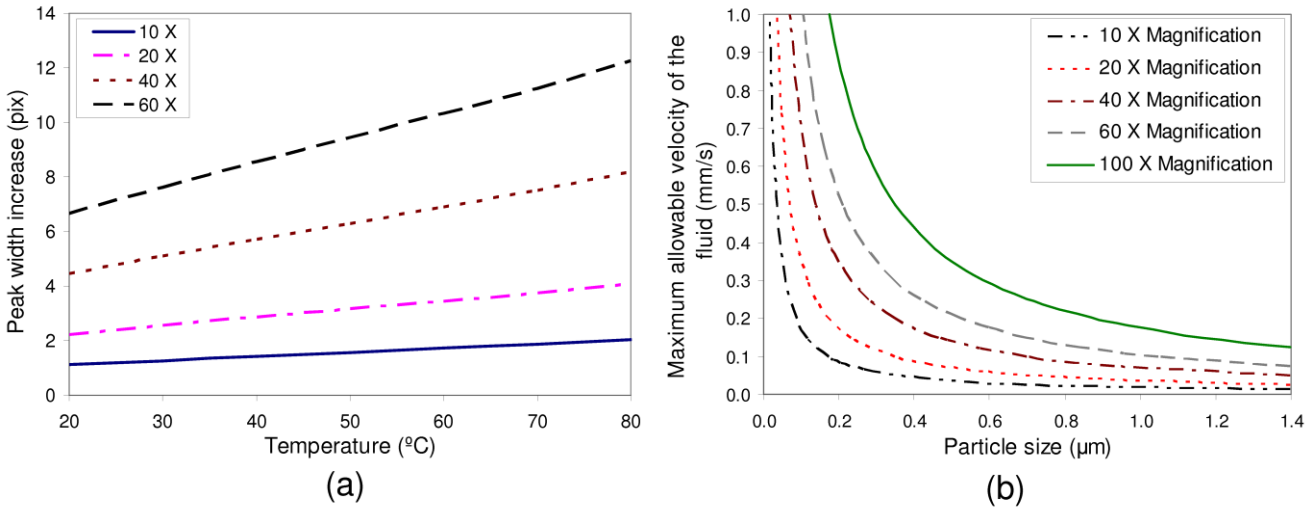

Figure 11 (a) The peak-width increase in pixels as a function of the magnification for the temperature range of 20ºC - 80ºC. (b) The maximum allowable velocity of the fluid as a function of the size of the particle for which the Brownian motion can still be resolved.